

# INVERSE MULTIVIEW II: MICROARCSECOND TRIGONOMETRIC PARALLAXES FOR SOUTHERN HEMISPHERE 6.7 GHz METHANOL MASERS G232.62+00.99 AND G323.74–00.26

L. J. HYLAND,<sup>1</sup> M. J. REID,<sup>2</sup> G. OROSZ,<sup>1,3</sup> S. P. ELLINGSEN,<sup>1</sup> S. D. WESTON,<sup>4</sup> J. KUMAR,<sup>1</sup> R. DODSON,<sup>5</sup> M. J. ROIJA,<sup>6,5,7</sup> W. J. HANKEY,<sup>1</sup> P. M. YATES-JONES,<sup>1</sup> T. NATUSCH,<sup>4</sup> S. GULYAEV,<sup>4</sup> K. M. MENTEN,<sup>8</sup> AND A. BRUNTHALER<sup>8</sup>

<sup>1</sup>*School of Natural Sciences, University of Tasmania, Private Bag 37, Hobart, Tasmania 7001, Australia*

<sup>2</sup>*Center for Astrophysics | Harvard & Smithsonian, Cambridge, MA 02138, USA*

<sup>3</sup>*Joint Institute for VLBI ERIC, Oude Hoogeveensedijk 4, 7991PD Dwingeloo, Netherlands*

<sup>4</sup>*Institute for Radio Astronomy and Space Research, Auckland University of Technology, 120 Mayoral Drive, Auckland 1010, New Zealand*

<sup>5</sup>*ICRAR, M468, The University of Western Australia, 35 Stirling Hwy, Crawley, Western Australia, 6009*

<sup>6</sup>*CSIRO Astronomy and Space Science, PO Box 1130, Bentley WA 6102, Australia*

<sup>7</sup>*Observatorio Astronómico Nacional (IGN), Alfonso XII, 3 y 5, 28014 Madrid, Spain*

<sup>8</sup>*Max-Planck-Institut fr Radioastronomie, Auf dem Hgel 69, D-53121 Bonn, Germany*

## ABSTRACT

We present the first results from the Southern Hemisphere Parallax Interferometric Radio Astrometry Legacy Survey (S $\pi$ RALS): 10 $\mu$ as-accurate parallaxes and proper motions for two southern hemisphere 6.7 GHz methanol masers obtained using the inverse MultiView calibration method. Using an array of radio telescopes in Australia and New Zealand, we measured the trigonometric parallax and proper motions for the masers associated with the star formation regions G232.62+00.99 of  $\pi = 0.610 \pm 0.011$  mas,  $\mu_x = -2.266 \pm 0.021$  mas y<sup>−1</sup> and  $\mu_y = 2.249 \pm 0.049$  mas y<sup>−1</sup>, which implies its distance to be  $d = 1.637 \pm 0.029$  kpc. These measurements represent an improvement in accuracy by more than a factor of 3 over the previous measurements obtained through Very Long Baseline Array observations of the 12 GHz methanol masers associated with this region. We also measure the trigonometric parallax and proper motion for G323.74–00.26 as  $\pi = 0.364 \pm 0.009$  mas,  $\mu_x = -3.239 \pm 0.025$  mas y<sup>−1</sup> and  $\mu_y = -3.976 \pm 0.039$  mas y<sup>−1</sup>, which implies a distance of  $d = 2.747 \pm 0.068$  kpc. These are the most accurate measurements of trigonometric parallax obtained for 6.7 GHz class II methanol masers to date. We confirm that G232.62+00.99 is in the Local arm and find that G323.74–00.26 is in the Scutum-Centaurus arm. We also investigate the structure and internal dynamics of G323.74–00.26.

*Keywords:* astrometry - proper motions, parallaxes; masers - methanol; techniques - Very Long Baseline Interferometry

## 1. INTRODUCTION

Measuring the trigonometric parallax (hereafter ‘parallax’) and the proper motion of stars or star-forming regions that trace the motion of interstellar gas, is the best method to accurately determine the structure and kinematics of the Milky Way. Parallax measurements at radio-frequencies have the advantage of not being obscured by dust, and can therefore probe much deeper into the disk of the Galaxy than those at optical frequencies.

Very Long Baseline Interferometry (VLBI) has been demonstrated to be able to achieve parallax accuracies of

$\pm 10 \mu$ as and therefore measure objects at a distance of 10 kpc with 10% accuracy (Reid & Honma 2014). Thus far, this level of accuracy has been almost exclusively achieved at radio-frequencies above 10 GHz and with homogeneous telescope arrays (e.g. the Very Long Baseline Array (VLBA)). At lower frequencies, uncompensated dispersive delays from the ionosphere can cause large systematic and direction-dependant errors (Rioja et al. 2017; Reid et al. 2017; Rioja & Dodson 2020).

MultiView (hereafter ‘direct MV’; Rioja et al. 2017), has been shown to give astrometric accuracies approaching values determined by the thermal noise. A new variation called inverse MultiView (iMV) has recently been

developed that allows additional robust calibration of short-timescale quasi-random phases changes at the position of that target, for target-calibrator separations of up to  $7^\circ$  at 8.3 GHz (Hyland et al. 2022).

The Southern Hemisphere Parallax Interferometric Radio Astrometry Legacy Survey (S $\pi$ RALS; Hyland 2021) is an extension of the Bar and Spiral Structure Legacy Survey (BeSSeL; Brunthaler et al. 2011; Reid et al. 2009b, 2014, 2019) and VLBI Exploration of Radio Astrometry (VERA; VERA Collaboration et al. 2020), with the aim to obtain information on the structure of the Milky Way for those regions exclusively visible from the southern hemisphere. S $\pi$ RALS targets 6.7 GHz methanol masers (Menten 1991), which are known to exclusively trace high-mass star formation (Minier et al. 2001; Ellingsen 2007; Breen et al. 2013). At these relatively low frequencies, the iMV approach can greatly improve the calibration of the dispersive delays due to the ionosphere.

In this paper, we demonstrate the calibration capabilities of iMV by measuring  $10\mu\text{s}$ -accurate parallaxes of two 6.7 GHz methanol masers. In Section 2 we describe target and calibrator selection, and observations. In Section 3 we outline all data reduction and analysis, including iMV calibration and parallax fitting. Section 4 presents the results and Section 5 includes a discussion of our findings.

## 2. METHODS

### 2.1. Source Selection and Observations

We selected two class II 6.7 GHz masers from the Methanol Multibeam Catalogue (MMB; Caswell et al. 2010, 2011; Green et al. 2012; Breen et al. 2015), which our pilot observations revealed to have compact emission in at least one 2 kHz/ $0.087\text{ km s}^{-1}$  velocity channel. The first was G232.62+00.99 (MacLeod et al. 1992), a maser associated with the hyper-compact HII region G232.6+1.0. As this target is at a declination of  $-17^\circ$ , it is visible from both the northern and southern hemispheres. Consequently, this maser region had an existing parallax measurement from the BeSSeL project (at 12 GHz; Reid et al. 2009a). This allows a direct comparison of parallaxes measured by the BeSSeL survey and S $\pi$ RALS.

The second maser was G323.74–00.26 (MacLeod et al. 1992), one of the strongest 6.7 GHz methanol masers known, which has been exhibiting a peak flux density over 3000 Jy (while flares with flux density up to 5800 Jy have also been observed; Goedhart et al. 2004). This maser is at a declination of  $-56^\circ$  and hence only visible to southern hemisphere instruments. There have been numerous studies of the 6.7 GHz methanol maser emis-

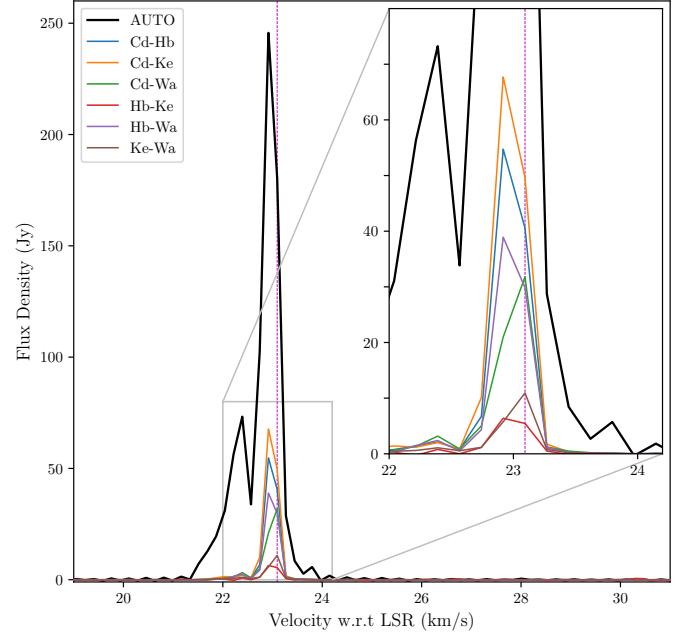


**Figure 1.** Auto- and cross-correlated spectra of G232.62+00.99 maser emission at epoch 6. Autocorrelated peak flux density (black line) is  $\sim 250$  Jy and Ke-Wa (the longest baseline) cross-correlated peak flux density is 10 Jy. The reference feature at  $23.08\text{ km s}^{-1}$  is indicated by the vertical magenta dashed line.

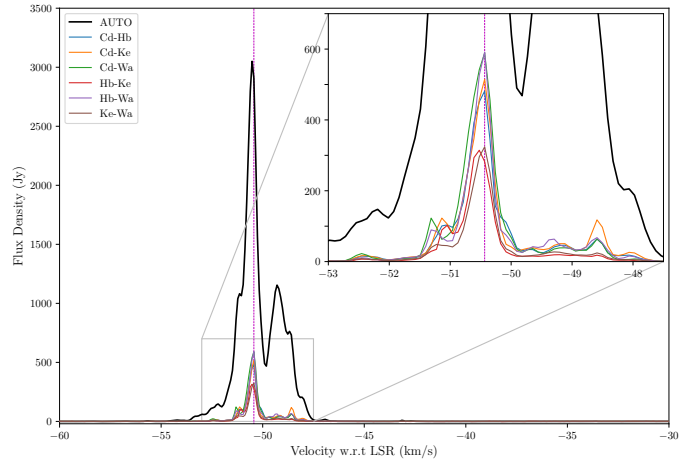


**Figure 2.** Auto- and cross-correlated spectra of G323.74–00.26 maser emission at epoch 4. Autocorrelated peak flux density is  $\sim 3500$  Jy and Ke-Wa cross-correlated flux density (brown line) peaks as 300 Jy at velocity  $-50.52\text{ km s}^{-1}$  (indicated by the vertical-dashed magenta line).

sion associated with this region (Norris et al. 1993, 1998; Phillips et al. 1998; Walsh et al. 2002; Ellingsen 2007; Vlemmings et al. 2011).

The spectra of G232.62+00.99 and G323.74–00.26 as detected by our array are shown in Figure 1 and Figure 2, respectively.

Hyland et al. (2022) showed that iMV with calibrators up to  $\approx 7^\circ$  separation from the target source can be successful at 8.3 GHz. At the lower frequency of 6.7 GHz, we chose calibrators separated by up to  $5.5^\circ$ . Allowing calibrators that are located up to this radius from a target provides many more bright and compact sources compared to the limitation that is usually applied for standard phase-referenced astrometric observations ( $< 2^\circ$ ).

Therefore for both of the target masers, we selected calibrators that met the criteria (in order of priority):

- unresolved flux density  $> 100$  mJy;
- within  $5.5^\circ$  separation;
- uniform directional sky sampling (with the target near the center).

For G232.62+00.99, we chose four calibrators separated by between 1 and  $4^\circ$  from the target (Table 1), originally from the catalog of Petrov et al. (2019). The fifth quasar at an angular separation of  $5.3^\circ$  (J0730–1141) was chosen as an electronic or “manual-phase” calibrator; however, its proximity to the target allowed incorporation into the iMV cycle.

For G323.74–00.26 we inferred the 6.7 GHz flux densities of calibrators from the available 8 GHz data (Petrov et al. 2019). Using the selection criteria above, we chose the 6 calibrators listed in Table 1. Note, there were no good<sup>1</sup> calibrators known within  $2^\circ$  of G323.74–00.26, and therefore standard phase referencing (PR) would have been difficult and likely to produce poor astrometric results.

The distribution of calibrators around the targets are shown in Figure 3, and Table 1 contains the calibrator positions and flux densities, listed in the order they were observed when nodding between the target and calibrator.

The structure of an individual observation session of nine hours was almost identical to that used by Hyland et al. (2022), with MultiView blocks bracketed by “geodetic-like” calibration blocks (Honma et al. 2007; Reid et al. 2009a; Reid & Honma 2014) and scans on bright compact calibrators. We observed seven epochs over a period of 1.5 years for G232.62+00.99 and seven epochs spanning 1 year for G323.74–00.26. The dates of

observations were chosen to sample near the extremes of the parallax oscillation in right ascension (R.A.) in order to optimize the accuracy to which the observations can measure the parallax. We refer to these maxima as “parallax seasons”.

## 2.2. Array, Frequency and Correlation

The array used for these observations is shown in Figure 4, comprising the University of Tasmania telescopes Ceduna 30m (McCulloch et al. 2005), Hobart 12m and Katherine 12m (Lovell et al. 2013), and the Auckland University of Technology telescope Warkworth 30m (Woodburn et al. 2015). This array has a maximum baseline length of 4750 km.

We recorded data at 1024 Gbps in dual polarisation, Nyquist sampled at 2-bits per sample, over the frequency range 6580–6708 GHz. The Ceduna 30m and Warkworth 30m antennas recorded right and left ( $\mathcal{R}, \mathcal{L}$ ) circular polarisations while Hobart 12m and Katherine 12m recorded horizontal and vertical ( $\mathcal{H}, \mathcal{V}$ ) linear polarizations.

Baseband data were correlated using DiFX-2 (Deller et al. 2011) in two passes: all sources were correlated over the full recorded frequency range with 0.5 MHz frequency channels, and the iMV blocks were correlated in a 4 MHz “zoom” band approximately centered on the frequency of the maser emission. The zoom band data for G232.62+00.99 were correlated to give frequency channels of 4 kHz, corresponding to velocity channels of  $0.174 \text{ km s}^{-1}$ ; for G323.74–00.26 we used frequency channels of 2 kHz giving velocity channels of  $0.087 \text{ km s}^{-1}$ .

In order to create valid FITS files from our mixed polarisation (i.e.  $\mathcal{HR}, \mathcal{VR}, \mathcal{HL}, \mathcal{VL}, \mathcal{RR}, \mathcal{LL}, \mathcal{RL}, \mathcal{LR}$ ) data (in *difx2fits*), we treated Hobart 12m and Katherine 12m  $\mathcal{H}$  as  $\mathcal{R}$  and  $\mathcal{V}$  as  $\mathcal{L}$  in our correlation. This approach was required as we were unsuccessful at converting the mixed polarisation products to a pure circular basis, owing to a lack of understanding of the complex apparent feed rotation characteristics of the Warkworth 30m (see Section 3.2). This reduced the amplitudes of mixed polarization products by  $\sqrt{2}$  (for an unpolarized source). Methanol masers at 6.7 GHz are known to exhibit low linear (typically 1.0–2.5%, max 17%) and circular polarization (typically 0.5–0.75%, max 6%; Surcis et al. 2022), and because of the low intrinsic polarization we did not see any adverse effects on our astrometric accuracy.

## 3. DATA REDUCTION AND ANALYSIS

### 3.1. Preliminary reduction

<sup>1</sup> Those exhibiting a flux density greater than 100 mJy, with positions known to better than 0.3 mas and/or with little to no extended structure.

**Table 1.** Target maser and calibrator QSO *correlated* positions, angular separations and flux densities. QSOs are ordered in the sequence that they were observed. **Columns:** Target maser and calibrator QSO (1-2) name, right ascension and declination position (3-4), angular separation in right ascension and declination (5-6), total separation (7), and flux density (8).

Source Name		R.A.	Dec.	Separation			Flux
Target	Calibrator	(J2000)	(J2000)	$\Delta\alpha \cos \delta_T$	$\Delta\delta$	$\theta_{\text{sep}}$	Density
Maser	QSOs	<i>h m s</i>	$^{\circ} \text{ } ' \text{ } ''$	( $^{\circ}$ )	( $^{\circ}$ )	( $^{\circ}$ )	(Jy)
G232.62+00.99		07 32 09.78	−16 58 12.80				$\sim 20^{\text{a}}$
	J0735−1735	07 35 45.812460	−17 35 48.50242	0.86	−0.62	1.06	0.10
	J0725−1904	07 25 50.165557	−19 04 19.07419	−1.51	−2.10	2.58	0.15
	J0729−1320	07 29 17.817692	−13 20 02.27125	−0.68	3.64	3.70	0.12
	J0748−1639	07 48 03.083813	−16 39 50.25355	3.80	0.31	3.81	0.30
	J0730−1141	07 30 19.112473	−11 41 12.60061	−0.44	5.28	5.30	3.18
G323.74−00.26		15 31 45.45	−56 30 50.10				$\sim 300^{\text{b}}$
	J1534−5351	15 34 20.660723	−53 51 13.42272	0.36	2.66	2.68	0.13 <sup>c</sup>
	J1600−5811	16 00 12.377460	−58 11 02.96855	3.92	−1.67	4.18	0.32 <sup>c</sup>
	J1524−5903	15 24 51.122912	−59 03 39.71702	−0.95	−2.55	2.71	0.06 <sup>c</sup>
	J1512−5640	15 12 55.819395	−56 40 30.64300	−2.60	−0.16	2.60	0.20 <sup>c</sup>
	J1515−5559	15 15 12.672909	−55 59 32.83823	−2.28	0.52	2.36	0.26 <sup>c</sup>
	J1511−5203	15 11 08.926191	−52 03 47.25032	−2.84	4.45	5.37	0.05 <sup>c</sup>

<sup>a</sup>Flux density of +23.09 km s<sup>−1</sup> channel at epoch 6.

<sup>b</sup>Flux density of −50.52 km s<sup>−1</sup> channel at epoch 4.

<sup>c</sup>Unresolved flux density at 8.4 GHz.

We calibrated correlated data in a similar manner to Hyland et al. (2022), with a few changes to account for dual-polarization/spectral line data, and the targets may have significant positional changes over the year(s). Briefly, using *AIPS* /ParselTongue (Greisen 1990, 2003; Kettenis et al. 2006) the additional steps to calibrate the data was as follows:

1. Apparent feed rotation corrections were applied to the dual polarisation data with task CLCOR/PANG (see Section 3.2 for a detailed discussion of the complex correction needed for the Warkworth 30m antenna).
2. Source position shifts (to improve relative positions among the sources) were applied with task CLCAL/ANTP.
3. Tasks SETJY/CVEL were used to correct for the Earth’s (rotation and orbital) Doppler shift, ensuring that the maser spectra were aligned in frequency during and across epochs.
4. A maser channel was selected to be the phase reference and the task FRING was used to solve for the phase and rate on that single channel. The criteria for channel selection was maximum flux den-

sity on the long Katherine 12m–Warthworth 30m baseline. This was applied to all sources by the task CLCAL.

5. Calibrations were applied to all data and the visibilities for the continuum sources were averaged in frequency using the task SPLIT
6. The calibrators were imaged using the IMAGR task. The position offset was determined for each calibrator and the weighted offsets of all calibrators were assumed to reflect a position error in the reference maser spot. Individual calibrator source offsets were used to refine their positions *relative* to the new maser position. These position corrections were measured for each observing season and applied to each source in Step 2. *Important note:* the final calibrator positions were required to be consistent for all epochs.
7. The calibrators were averaged in frequency using the task SPLAT and the phase was measured with the CALIB task. The solutions were output and used for iMV fitting (described in Section 3.3)

### 3.2. Warkworth 30m Apparent Feed Rotation Correction

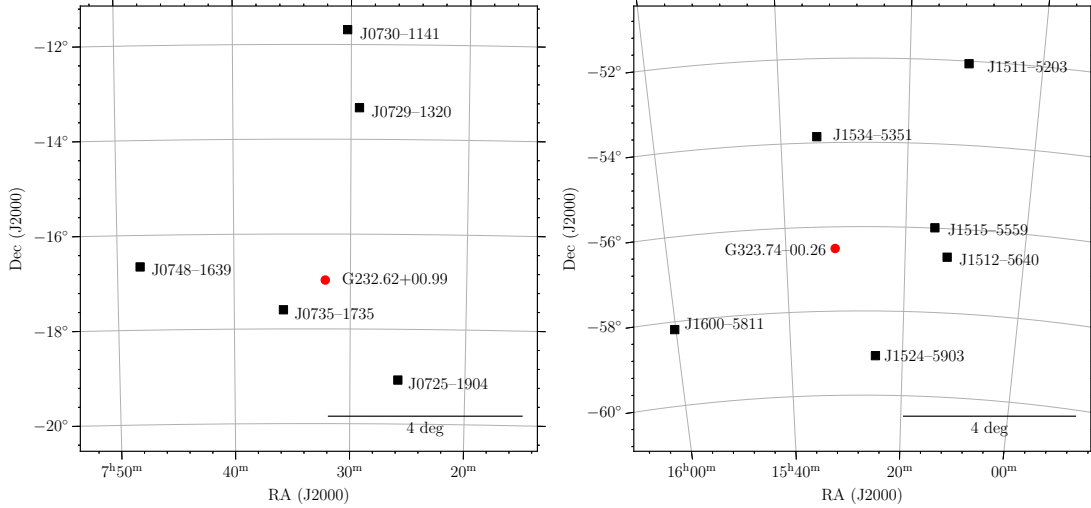


**Figure 3.** Sky distributions of target masers (red dot) and calibrators (black squares). **Left:** Target maser G232.62+00.99 with 5 calibrator QSOs. The smallest calibrator separation is  $1.06^\circ$  (J0735-1735) and the largest is  $5.30^\circ$  (J1730-1141). **Right:** Target maser G323.740-0.263 with 6 calibrator QSOs. Smallest calibrator separation is  $2.36^\circ$  (J1515-5559) and largest is  $5.37^\circ$  (J1511-5203).

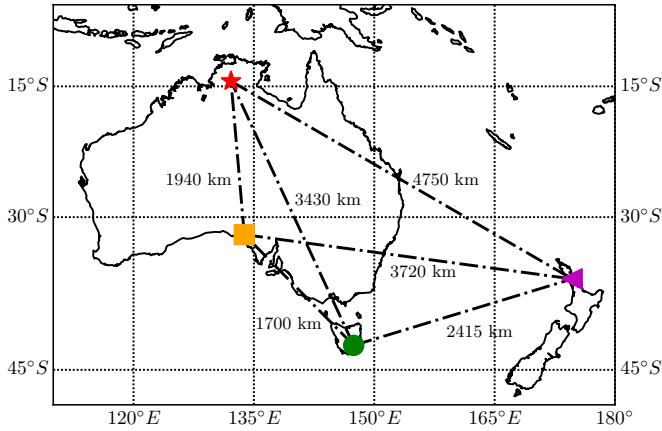


**Figure 4.** VLBI array used for these observations, with University of Tasmania telescopes Ceduna 30m (orange square), Hobart 12m (green circle), Katherine 12m (red star) and Auckland University of Technology telescope Warkworth 30m (purple triangle). Baselines are indicated with dash-dotted lines and baseline lengths are given next to corresponding baselines.

The Warkworth 30m antenna is a Naysmith wheel-on-track antenna with a beam waveguide design (Petrov et al. 2015). The physical feed does not rotate when the antenna moves and a system of four mirrors directs the beam into the receiver; i.e. a Beam Wave-Guide system, which are not uncommon for converted telecom antennas (Warkworth NZ, Yamaguchi JP, Nkutunse GH, etc.). At the time of analysis, the standard *AIPS* task CLCOR/PANG did not include corrections for this type of focus. In order to combine the dual polarisation data

we needed to correct for the phase introduced as the antenna moves in azimuth and elevation.

We found the phase correction,  $\varphi$ , that accounts for the apparent feed rotation is:

$$\varphi = -q - \mathcal{A} + \mathcal{E} \quad (1)$$

where  $q$  is the parallactic angle,  $\mathcal{A}$  is the azimuth angle (measured North through East), and  $\mathcal{E}$  is the elevation angle. Subtracting  $\varphi$  from the RCP signal ( $\mathcal{R}$ ) and adding it to the LCP signal ( $\mathcal{L}$ ) phase corrects the visibility data for the apparent feed rotation, allowing the  $\mathcal{R}$  and  $\mathcal{L}$  data to be averaged before fringe fitting on the maser and increasing the S/N by a factor of  $\sqrt{2}$  (the feed correction has subsequently been added to the CLCOR task and the technical details are described in Dodson & Rioja 2022).

### 3.3. *iMV* Calibration

Given the existence of occasional phase wraps in the 8.3 GHz experiments described by Hyland et al. (2022), we expected a similar or greater number to be present at 6.7 GHz. The residual path delay,  $\Delta\tau$ , for a dispersive medium like the ionosphere scales with frequency,  $\nu$ , as  $\nu^{-2}$ . Interferometer phase,  $\phi$ , is given by  $\phi = \Delta\tau \nu$ , and thus the effect on phase scales as  $\nu^{-1}$ . Therefore, scaling from 8.3 GHz to 6.7 GHz should lead to a 20% increase in phase shifts (assuming the same value for the residual total electron content TEC). This implies there are likely to be an increased number of phase wraps in our 6.7 GHz data compared to those seen by Hyland et al. (2022).

In order to unwrap the phases, we took the minimum difference of phase between consecutive scans on the



same calibrator when adding trial values of 360, 0, and  $-360^\circ$ . Additionally, all phases were minimized relative to a common time at the center of the track, where the delay errors due to residual tropospheric and ionospheric errors are expected to be at a minimum.

Once unwrapped, the phase data on each scan was fit with the least squares method to a model for a 2D plane (see Equation 5 from Hyland et al. (2022)) and the interpolated phase at the origin was subtracted from the maser visibility data using the task CLCAL.

The maser reference channel was then imaged using the *AIPS* task IMAGR, and the brightness distribution was fitted with a Gaussian model using the task JMFIT in order to measure the astrometric offsets ( $x_m, y_m$ ) from the original phase center in Table 2.

### 3.4. Position shifting and parallax fitting

In order to minimize phase wraps (see the previous section), the (moving) maser position was updated at each observing season. In order to put the measured positions back into a stationary reference frame, one must undo these shifts before fitting the parallax and proper motion. To achieve this, we first calculated the average shift (from the correlated position) and used this as our reference position:  $\bar{x}_T, \bar{y}_T$ . We then calculated the offset from this reference position at each epoch (e.g.  $x_T - \bar{x}_T$ ) and added it to the measured maser offset from the synthesized images ( $x_m, y_m$ ). This gave the total offset from the reference position over time ( $x_{\text{tot}}, y_{\text{tot}}$ ). These values are given in Table 2.

We fit the ( $x_{\text{tot}}, y_{\text{tot}}$ ) data using the model of Equation 2 in the Appendix with variance-weighted least-squares to determine the parallax ( $\pi$ ), and the proper motions ( $\mu_x, \mu_y$ ). Since astrometric uncertainty is usually dominated by systematic error, whose magnitude is not known *a priori*, we added “error floors” to the  $x$  and  $y$  data in quadrature. We independently varied these error floors to achieve a chi-squared per degree of freedom of unity for each coordinate. This approach is widely used in maser astrometry and is considered the most reliable method for estimating the uncertainties in  $\pi, \mu_x, \mu_y$  (Reid et al. 2009a). The models as fit to the astrometric data for each target are shown in Figure 5 and Figure 6.

## 4. RESULTS

Using iMV, we measure the parallax and proper motion of the 6.7 GHz emission in G232.62+00.99 to be  $\pi = 0.610 \pm 0.011$  mas,  $\mu_x = -2.266 \pm 0.021$  mas  $\text{y}^{-1}$ , and  $\mu_y = 2.249 \pm 0.049$  mas  $\text{y}^{-1}$ . This yields a distance of  $d = 1.639 \pm 0.030$  kpc (i.e. parallax inversion  $d = 1/\pi$  with symmetric errors  $\sigma_d = \sigma_\pi/\pi^2$ ). For

G323.74–00.26, we measure a parallax of  $\pi = 0.364 \pm 0.009$  mas and proper motion of  $\mu_x = -3.239 \pm 0.025$  and  $\mu_y = -3.976 \pm 0.039$  mas  $\text{y}^{-1}$ , yielding a distance of  $d = 2.747 \pm 0.068$  kpc.

In order to evaluate the astrometric improvement of iMV compared to standard (inverse) phase referencing using a single-calibrator, we also estimated parallaxes relative to each quasar in each cluster. We find that the parallaxes based on individual calibrators in the G232.62+00.99 cluster range from 0.433 to 0.636 mas and in the G323.74–00.26 cluster range from 0.294 to 0.484 mas. These results are consistent with systematic parallax shifts of magnitude  $\sim 0.05$  mas per degree of calibrator angular offset found by Reid et al. (2017). All of the parallax and proper motion results are tabulated in Table 3.

## 5. DISCUSSION

The parallax and proper motion of the 12 GHz methanol emission in G232.62+1.0 was measured with the VLBA between October 2005 and March 2007 to be  $\pi = 0.596 \pm 0.035$  mas,  $\mu_x = -2.17 \pm 0.06$  mas  $\text{y}^{-1}$ ,  $\mu_y = 2.09 \pm 0.46$  mas  $\text{y}^{-1}$  (Reid et al. 2009a). Compared to this previous measurement, the parallax and proper motions of the 6.7 GHz methanol and 12 GHz methanol agree within the quoted uncertainties, with the obvious difference being that the new estimate is 3-times more accurate for  $\pi$  and  $\mu_x$  and an order of magnitude more accurate for  $\mu_y$ .

It should be noted that the previous measurement was subject to issues that limited the VLBA: namely the source was observed at very low elevations and, the 12 GHz emission was resolved and only the inner five VLBA antennas were used, limiting the maximum baseline length to 1500 km (compared to the maximum baseline we use of 4750 km). Accounting for the latter by simply dividing the previous parallax measurement uncertainty by  $\sim 3$  reduces it to  $\pm 12 \mu\text{as}$ . This indicates that we were able to successfully calibrate the delays (primarily the ionosphere) at 6.7 GHz to at least the same levels as could be achieved at 12 GHz, if not better.

The last southern hemisphere 6.7 GHz methanol maser parallaxes were measured by Krishnan et al. (2015, 2017) on the Long Baseline Array – another southern hemisphere VLBI array that has common telescopes with what we have used. These measurements were plagued by uncompensated dispersive delays, leading to parallaxes with accuracy between 50 – 110  $\mu\text{as}$ . Compared to the  $\sim 10 \mu\text{as}$  parallaxes we have measured, we can see there has been a marked improvement owing to MV techniques.

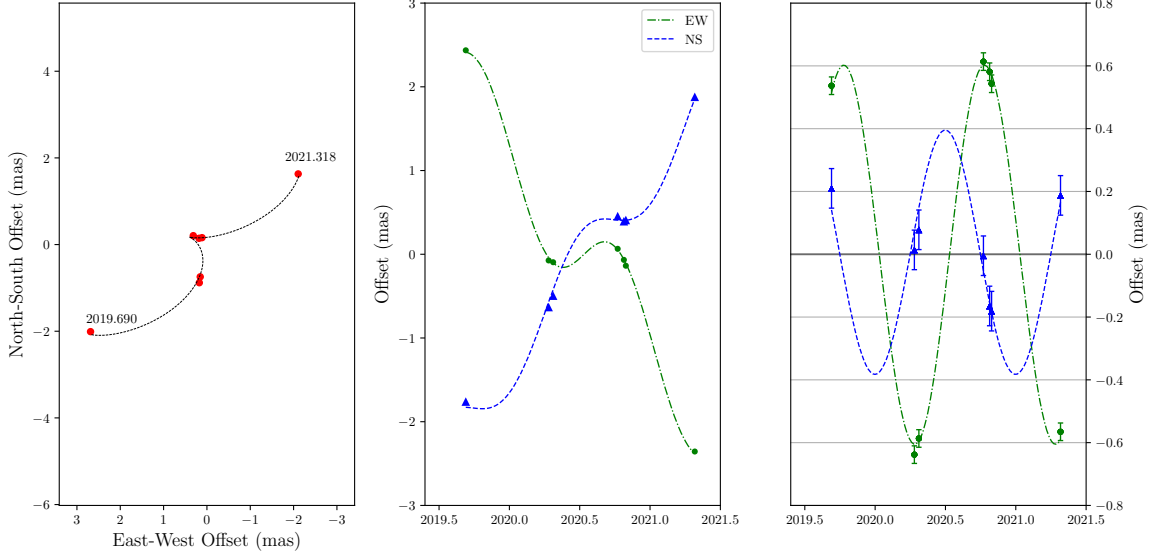


**Figure 5.** Parallax and proper motion modelling of G232.62+00.99 velocity channel  $v = 23.08 \text{ km s}^{-1}$ . **Left:** Total sky position change over the full observation period. **Middle:** Decomposition of sky motion into East-West (green dot-dashed) and North-South (blue dashed) motion over time. **Right:** Proper-motion subtracted sky motion over time. Error bars include  $1\sigma$  error floors for each coordinate of  $28\mu\text{as}$  and  $62\mu\text{as}$  for the EW and NS directions respectively.

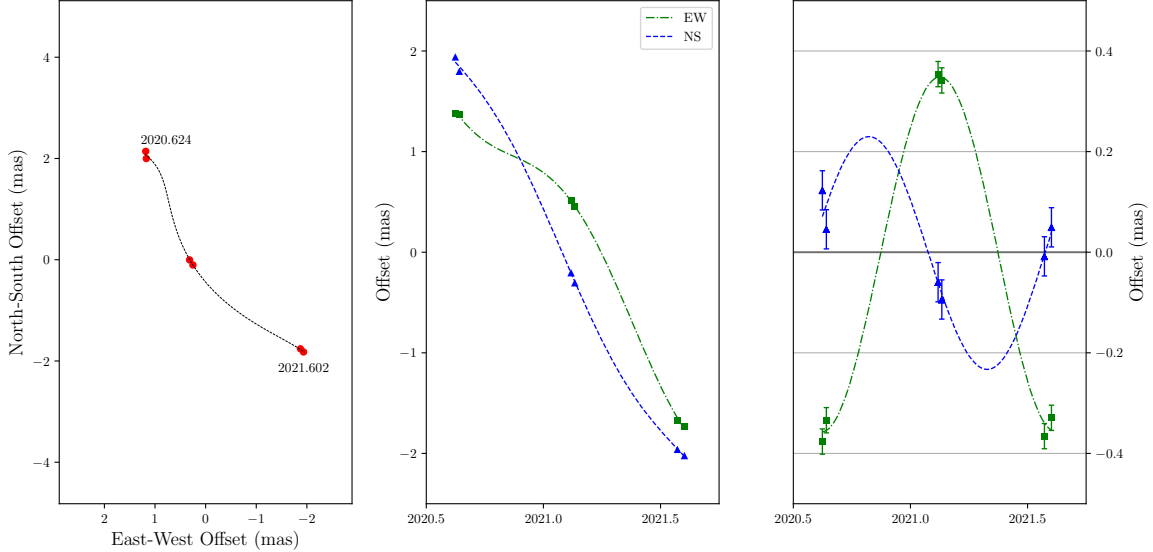


**Figure 6.** Parallax and proper motion modelling of G233.74-00.26 velocity channel  $v = -50.52 \text{ km s}^{-1}$ . **Left:** Total sky position change over full observation period. **Middle:** Decomposition of sky motion into East-West (green dot-dashed) and North-South (blue dashed) motion over time. **Right:** Parallax motion (i.e. proper-motion subtracted) over time. Error bars show independent  $1\sigma$  error floors for each direction as  $25\mu\text{as}$  and  $39\mu\text{as}$  for the EW and NS directions respectively.

G232.62+00.99 well-matches the  $(l, b)$  coordinates of the Local arm as traced by Reid et al. (2019). The centroid velocity of the associated 6.7 GHz masers is near  $23 \text{ km s}^{-1}$ , which compares reasonably with  $17 \text{ km s}^{-1}$  fitted to Local arm sources nearby in angle. The small difference can be easily accounted for with the expected Virial motions of within giant molecular clouds.

The center of the Local arm at longitude  $232^\circ$  is at a distance of 0.83 kpc, and the estimated Gaussian  $1\sigma$  width of an arm at a Galactocentric radius of 9 kpc is 0.4 kpc (Reid et al. 2019). At our measured distance of 1.64 kpc, this places G232.62+00.99 at 0.81 kpc (or about  $2\sigma$ ) from the arm center. Since this source is at one end (at Galactic azimuth  $-8^\circ$ ) of sources with measured parallaxes used to trace the Local arm, it

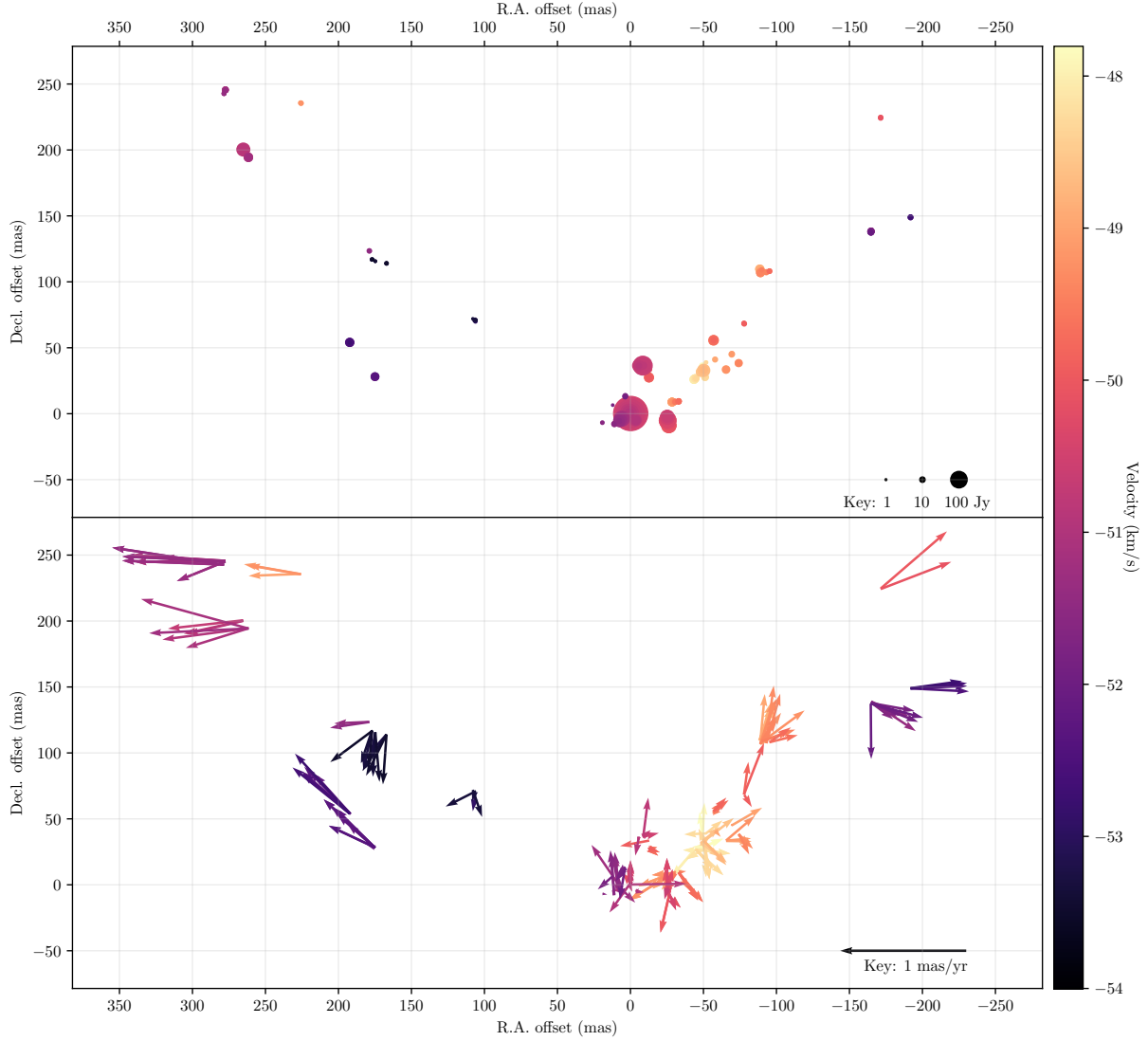


**Figure 7.** Map of methanol maser spots and their relative proper motions. Features shown were detected in  $\geq 5$  epochs.

could be that the pitch angle fitted over that azimuth range extending to the other end (azimuth  $+34^\circ$ ) should be increased slightly. Interestingly, however, there is a “bridge” of gas seen in HI starting at  $(l, V_{lsr}) = (232^\circ, 20 \text{ km s}^{-1})$  and connecting to the Perseus arm at  $(242^\circ, 70 \text{ km s}^{-1})$  (see Fig. 12 of Reid et al. 2016). Possibly, G232.62+00.99 is associated with this bridge.

G323.74–00.26 is clearly associated with the Scutum-Centaurus spiral arm, since its  $(l, b, V_{lsr})$  coordinates of  $(323^\circ 74', -0^\circ 26', -50 \text{ km s}^{-1})$  compare very well with the arm model of  $(323^\circ, -0^\circ 01', -53 \text{ km s}^{-1})$  of Reid et al. (2019). That model places the center of the arm at this longitude at a distance of 3.2 kpc, which is about 0.45 kpc more distant than our parallax. At a Galactocentric radius of 6.1 kpc the arm width estimate of Reid et al. (2019) is 0.26 kpc, placing this source  $1.7\sigma$  from the center. However, given that at present very

few southern sources have accurate parallax measurements, this is not surprising, since the precise location of the Centaurus arm segment might be fairly uncertain at this time.

The G323.74–00.26 maser emissions arises from quite a large number of emission regions (‘spots’). By imaging these spots over all epochs and tracking any changes in position, we can infer the *internal motions* of the whole maser region. Figure 7 shows the positions of bright spots and their apparent motions over time. We have subtracted the average motion of  $\mu_{x_{int}} = 0.00 \pm 0.02$  and  $\mu_{y_{int}} = -0.198 \pm 0.012 \text{ mas y}^{-1}$  in the R.A. and declination directions respectively. If the distribution of measured spot motion is near-isotropic, then this average will be close to the (opposite of the) internal motion of the reference feature. Therefore we also subtracted this motion from the measured proper motion



**Table 2.** Epochs of VLBI observations and astrometric positions.

Target	Epoch	Date	Target Shift		w.r.t Ref. pos		Meas. Offset		Total Offset	
			$x_T$	$y_T$	$x_T - \bar{x}_T$	$y_T - \bar{y}_T$	$x_m$	$y_m$	$x_{\text{tot}}$	$y_{\text{tot}}$
			(mas)	(mas)	(mas)	(mas)	(mas)	(mas)	(mas)	(mas)
G232.62+00.99	1	2019 Sep 09	20.82	242.083	2.7	-2.2	-0.028	0.177	2.692	-2.023
	2	2020 Apr 12	18.42	243.583	0.3	-0.7	-0.146	-0.203	0.154	-0.903
	3	2020 Apr 24	18.42	243.583	0.3	-0.7	-0.212	-0.263	0.088	-0.963
	4	2020 Oct 09	18.22	244.383	0.1	0.1	0.208	0.110	0.308	0.210
	5	2020 Oct 25	18.22	244.383	0.1	0.1	-0.009	0.093	0.091	0.193
	6	2020 Oct 30	18.22	244.383	0.1	0.1	-0.043	0.063	0.057	0.163
	7	2021 Apr 26	16.22	245.883	-1.9	1.6	-0.203	-0.017	-2.103	1.583
	8	2021 May 03	16.22	245.883	-1.9	1.6	-0.006	-0.162	-1.987	1.582
<i>Ref. pos (<math>\bar{x}_T, \bar{y}_T</math>):</i>			18.12	244.283						
G323.74-00.26	1	2020 Aug 15	-187.1	-177.7	1.5	1.9	-0.268	0.239	1.232	2.139
	2	2020 Aug 21	-187.1	-177.7	1.5	1.9	-0.281	0.098	1.219	1.998
	3	2021 Feb 12	-188.3	-179.6	0.3	0.0	0.058	0.012	0.358	-0.012
	4	2021 Feb 18	-188.3	-179.6	0.3	0.0	-0.009	-0.143	0.291	-0.143
	5	2021 Feb 22	-188.3	-179.6	0.3	0.0	-0.020	-0.114	0.280	-0.114
	6	2021 Jul 28	-190.4	-181.4	-1.8	-1.8	-0.031	0.037	-1.831	-1.763
	7	2021 Aug 08	-190.4	-181.4	-1.8	-1.8	-0.089	-0.033	-1.889	-1.833
<i>Ref. pos (<math>\bar{x}_T, \bar{y}_T</math>):</i>			-188.6	-179.6						

of the reference feature measured with respect to the quasars (Table 3) to obtain an estimate of the absolute motion of the region giving  $\mu_{x_{\text{tot}}} = -3.2 \pm 0.4$  and  $\mu_{y_{\text{tot}}} = -4.2 \pm 0.4$  mas  $\text{y}^{-1}$ . Here we have also added an additional uncertainty of  $0.4$  mas  $\text{y}^{-1}$  in quadrature (equivalent to  $5$  km  $\text{s}^{-1}$  at the measured distance) to account for the likelihood that the spots do not have an isotropic velocity distribution. There does not seem to be significant evidence in favour of an edge-on disk structure as has been suggested for methanol masers (e.g. Phillips et al. 1998), and the structure and internal motions instead suggest that the maser spot distribution may be part of a bow shock.

The peculiar (non-circular) motion of G323.74-00.26 about the Galactic Center of mass can be calculated from its measured 6-dimensional phase-space values. Adopting a  $V_{\text{lsr}} = 50.5 \pm 5.0$  km  $\text{s}^{-1}$  and the rotation curve of Reid et al. (2019), we find  $(U_p, V_p, W_p) = (-5, -1, -8)$  km  $\text{s}^{-1}$ , where  $U_p$  is toward the Galactic center at the position of the source,  $V_p$  is in the direction of Galactic rotation, and  $W_p$  is toward the North Galactic Pole. Uncertainties from measurement error are  $\pm 5$  km  $\text{s}^{-1}$  in each coordinate, so G323.74-00.26 has the very small peculiar motion typical of a young high-mass star.

Comparing the parallax and proper motion results from iMV with a group of calibrators to standard (inverse) phase referencing with a single calibrator (Table 3), we find that iMV is at least a factor of two better in accuracy. In Hyland et al. (2022), per-epoch positional uncertainties of  $\pm 20$   $\mu\text{as}$  were achieved at 8.3 GHz for calibrator separations  $< 7^\circ$  in both NS and EW directions. Here we report per-epoch positional uncertainties (determined from the error floor values) of  $\approx 26$   $\mu\text{as}$  in the EW direction and  $\approx 50$   $\mu\text{as}$  in the NS direction.

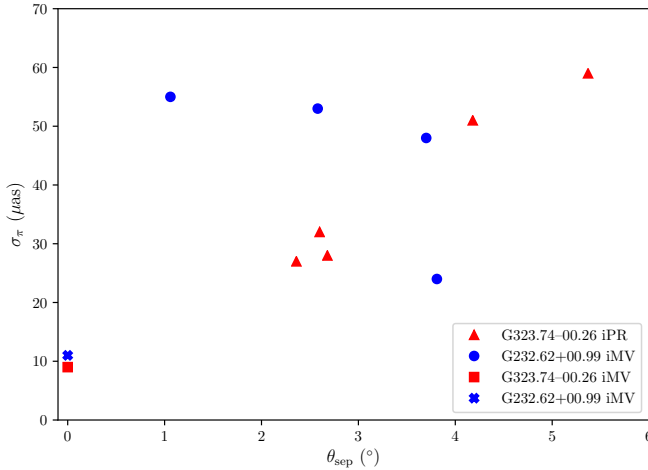
Figure 8 shows the iPR parallax accuracy as a function of total angular separation for both targets. The behaviour of the G323.74-00.26 iPR parallaxes is exactly as expected, where the error increases linearly with target-calibrator separation. This is not the case for G232.62+00.99, where the best residual fit to parallax comes from the furthest separated calibrator with an iPR result. This unusual behaviour of the parallax error vs. target-calibrator separation, and the systematic offsets seen from the iPR vs. iMV results for both masers, highlights the risk of relying on standard phase referencing at 6.7 GHz, and demonstrates that MV-techniques are critical for accurate astrometry at this frequency.

## 6. CONCLUDING REMARKS

**Table 3.** Trigonometric parallaxes and proper motions determined from iPR from the target maser, and iMV.

	Source	$\theta_{\text{sep}}$	$\pi$	$\mu_x$	$\mu_y$
Target	Background	( $^\circ$ )	(mas)	(mas y $^{-1}$ )	(mas y $^{-1}$ )
G232.62+00.99	J0735–1735	1.06	$0.523 \pm 0.055$	$-2.367 \pm 0.100$	$2.353 \pm 0.100$
	J0725–1904	2.58	$0.634 \pm 0.053$	$-2.221 \pm 0.098$	$2.155 \pm 0.204$
	J0729–1320	3.70	$0.636 \pm 0.048$	$-2.175 \pm 0.085$	$2.533 \pm 0.128$
	J0748–1639	3.81	$0.433 \pm 0.024$	$-2.252 \pm 0.043$	$2.958 \pm 0.142$
	J0730–1141 <sup>a</sup>	5.30	-		
	<i>iPR Mean</i>		$0.499 \pm 0.019$	$-2.249 \pm 0.034$	$2.507 \pm 0.065$
	<i>iMV w/ all</i>		$0.610 \pm 0.011$	$-2.266 \pm 0.021$	$2.249 \pm 0.049$
G323.74–00.26	J1515–5559	2.36	$0.359 \pm 0.027$	$-3.25 \pm 0.08$	$-4.01 \pm 0.10$
	J1512–5640	2.60	$0.374 \pm 0.032$	$-3.23 \pm 0.09$	$-3.83 \pm 0.25$
	J1534–5351	2.68	$0.437 \pm 0.028$	$-3.20 \pm 0.08$	$-3.89 \pm 0.15$
	J1524–5903 <sup>b</sup>	2.71	-		
	J1600–5811	4.18	$0.294 \pm 0.051$	$-3.06 \pm 0.14$	$-3.72 \pm 0.19$
	J1511–5203	5.37	$0.484 \pm 0.059$	$-3.57 \pm 0.18$	$-3.71 \pm 0.25$
	<i>iPR Mean</i>		$0.388 \pm 0.015$	$-3.23 \pm 0.04$	$-3.91 \pm 0.07$
	<i>iMV w/ all</i>		$0.364 \pm 0.009$	$-3.239 \pm 0.025$	$-3.976 \pm 0.039$
	<i>inc. int. mot.</i>			$-3.239 \pm 0.400$	$-4.174 \pm 0.400$

NOTE—iMV results attained using data from all QSOs.

<sup>a</sup>iPR from G232.62+00.99 to QSO J0730–1141 did not produce coherent maps at any epoch.<sup>b</sup>iPR from G323.74–00.26 to QSO J1524–5903 only produced coherent maps at three out of seven epochs.**Figure 8.** Parallax error vs. target-calibrator separation for iPR and iMV results. The iMV errors are taken to be at separation  $\sim 0^\circ$ .

We have used inverse MultiView to measure the parallax and proper motion of two 6.7 GHz class II methanol masers, with results approaching the highest accuracy ever achieved at this frequency.

As part of the S $\pi$ RALS project we will continue to measure the parallaxes and proper motions for southern hemisphere 6.7 GHz class II methanol masers to fill in the 4th quadrant to better trace the spiral arms of the Milky Way. For methanol masers that are too weak for iMV, we aim to use direct MV (Rioja et al. 2017).

#### DATA AND CODE AVAILABILITY

The data underlying this article will be shared on reasonable request to the corresponding author. The scripts and programs used for data reduction and calibration are available at <https://github.com/lucasjordan/spirals>.

#### ACKNOWLEDGEMENTS

This research was supported by the Australian Research Council (ARC) Discovery Grant DP180101061. We want to thank Mr. Brett Reid and Mrs. Bev Benson for maintaining and organizing the University of Tasmania radio telescopes. We acknowledge the Jawoyn, Paredarmerme, and Wirangu peoples as the traditional owners of the land siting the Katherine, Hobart, and Ceduna telescopes respectively. The Wark-

worth 30m radio telescope is funded and operated by the Auckland University of Technology; we would like to thank Mr. Lewis Woodburn for the maintenance and management of this facility to enable its involvement in this project. This research has made use of NASA's Astrophysics Data System Abstract Service. This research made use of [MaserDB.net](#), an online database of astrophysical masers ([Ladeyschikov et al. 2019](#)). This research made use of Astropy, a community-developed core Python package for Astronomy ([Astropy Collaboration et al. 2013, 2018](#)).

## APPENDIX

The model used to predict the position of the target  $(x, y)$  at any given time  $(t)$  relative to some reference

time  $(t_0)$  due to parallax  $(\pi)$  and proper motion  $(\mu_x, \mu_y)$  is as follows:

$$\begin{aligned} x &= \pi (Y \cos \alpha - X \sin \alpha) + \mu_x (t - t_0) \\ y &= \pi (Z \cos \delta - X \cos \alpha \sin \delta \\ &\quad - Y \sin \alpha \sin \delta) + \mu_y (t - t_0) \end{aligned} \quad (2)$$

where  $\alpha, \delta$  are the R.A. and Dec. of the target, and  $X, Y, Z$  is the Earth's position relative to the Sun at epoch  $t$  (as determined by the NOVAS subroutines; [Kaplan et al. 1989](#)). Since the NOVAS routines request  $t$  in MJD, the  $\mu$  values are returned in mas d<sup>-1</sup>.

## REFERENCES

- Astropy Collaboration, Robitaille, T. P., Tollerud, E. J., et al. 2013, [A&A](#), **558**, A33
- Astropy Collaboration, Price-Whelan, A. M., Sipőcz, B. M., et al. 2018, [AJ](#), **156**, 123
- Breen, S. L., Ellingsen, S. P., Contreras, Y., et al. 2013, [MNRAS](#), **435**, 524
- Breen, S. L., Fuller, G. A., Caswell, J. L., et al. 2015, [MNRAS](#), **450**, 4109
- Brunthaler, A., Reid, M. J., Menten, K. M., et al. 2011, [Astronomische Nachrichten](#), **332**, 461
- Caswell, J. L., Fuller, G. A., Green, J. A., et al. 2010, [MNRAS](#), **404**, 1029
- . 2011, [MNRAS](#), **417**, 1964
- Deller, A. T., Bricken, W. F., Phillips, C. J., et al. 2011, [PASP](#), **123**, 275
- Dodson, R., & Rioja, M. J. 2022, in eLBA memo 14
- Ellingsen, S. P. 2007, [MNRAS](#), **377**, 571
- Goedhart, S., Gaylard, M. J., & van der Walt, D. J. 2004, [MNRAS](#), **355**, 553
- Green, J. A., Caswell, J. L., Fuller, G. A., et al. 2012, [MNRAS](#), **420**, 3108
- Greisen, E. W. 1990, in Acquisition, Processing and Archiving of Astronomical Images, 125
- Greisen, E. W. 2003, in [Astrophysics and Space Science Library](#), Vol. 285, Information Handling in Astronomy - Historical Vistas, ed. A. Heck, 109
- Honma, M., Bushimata, T., Choi, Y. K., et al. 2007, [PASJ](#), **59**, 889
- Hyland, L. J. 2021, PhD thesis, School of Natural Sciences
- Hyland, L. J., Reid, M. J., Ellingsen, S. P., et al. 2022, [ApJ](#), **932**, 52
- Kaplan, G. H., Hughes, J. A., Seidelmann, P. K., Smith, C. A., & Yallop, B. D. 1989, [AJ](#), **97**, 1197
- Kettenis, M., van Langevelde, H. J., Reynolds, C., & Cotton, B. 2006, in Astronomical Society of the Pacific Conference Series, Vol. 351, Astronomical Data Analysis Software and Systems XV, ed. C. Gabriel, C. Arviset, D. Ponz, & S. Enrique, 497
- Krishnan, V., Ellingsen, S. P., Reid, M. J., et al. 2017, [MNRAS](#), **465**, 1095
- . 2015, [ApJ](#), **805**, 129
- Ladeyschikov, D. A., Bayandina, O. S., & Sobolev, A. M. 2019, [AJ](#), **158**, 233
- Lovell, J. E. J., McCallum, J. N., Reid, P. B., et al. 2013, [Journal of Geodesy](#), **87**, 527
- MacLeod, G. C., Gaylard, M. J., & Nicolson, G. D. 1992, [MNRAS](#), **254**, 1P
- McCulloch, P. M., Ellingsen, S. P., Jauncey, D. L., et al. 2005, [AJ](#), **129**, 2034
- Menten, K. M. 1991, [ApJL](#), **380**, L75
- Minier, V., Conway, J. E., & Booth, R. S. 2001, [A&A](#), **369**, 278
- Norris, R. P., Whiteoak, J. B., Caswell, J. L., Wieringa, M. H., & Gough, R. G. 1993, [ApJ](#), **412**, 222
- Norris, R. P., Byleveld, S. E., Diamond, P. J., et al. 1998, [ApJ](#), **508**, 275
- Petrov, L., de Witt, A., Sadler, E. M., Phillips, C., & Horiuchi, S. 2019, [MNRAS](#), **485**, 88
- Petrov, L., Natusch, T., Weston, S., et al. 2015, [PASP](#), **127**, 516
- Phillips, C. J., Norris, R. P., Ellingsen, S. P., & McCulloch, P. M. 1998, [MNRAS](#), **300**, 1131
- Reid, M. J. 2022, [AJ](#), **164**, 133
- Reid, M. J., Dame, T. M., Menten, K. M., & Brunthaler, A. 2016, [ApJ](#), **823**, 77
- Reid, M. J., & Honma, M. 2014, [ARA&A](#), **52**, 339

- Reid, M. J., Menten, K. M., Brunthaler, A., et al. 2009a, [ApJ](#), 693, 397
- Reid, M. J., Menten, K. M., Zheng, X. W., et al. 2009b, [ApJ](#), 700, 137
- Reid, M. J., Menten, K. M., Brunthaler, A., et al. 2014, [ApJ](#), 783, 130
- Reid, M. J., Brunthaler, A., Menten, K. M., et al. 2017, [AJ](#), 154, 63
- Reid, M. J., Menten, K. M., Brunthaler, A., et al. 2019, [ApJ](#), 885, 131
- Rioja, M. J., & Dodson, R. 2020, [A&A Rv](#), 28, 6
- Rioja, M. J., Dodson, R., Orosz, G., Imai, H., & Frey, S. 2017, [AJ](#), 153, 105
- Surcis, G., Vlemmings, W. H. T., van Langevelde, H. J., Hutawarakorn Kramer, B., & Bartkiewicz, A. 2022, [A&A](#), 658, A78
- VERA Collaboration, Hirota, T., Nagayama, T., et al. 2020, [PASJ](#), [arXiv:2002.03089 \[astro-ph.GA\]](#)
- Vlemmings, W. H. T., Torres, R. M., & Dodson, R. 2011, [A&A](#), 529, A95
- Walsh, A. J., Lee, J. K., & Burton, M. G. 2002, [MNRAS](#), 329, 475
- Woodburn, L., Natusch, T., Weston, S., et al. 2015, [PASA](#), 32, 17